Journal of
Applied Crystallography

ISSN 0021-8898

Received 29 November 2006
Accepted 14 March 2007

Operator-assisted harvesting of protein crystals using a universal micromanipulation robot

Robert Viola,[a] Peter Carman,[a] Jace Walsh,[a] Echo Miller,[a] Matthew Benning,[b] Daniel Frankel,[b] Alexander McPherson,[c] Bob Cudney[d] and Bernhard Rupp[c,e]*

[a]Square One Systems Design, Jackson Hole, WY 83002, USA, [b]Bruker Analytical X-ray Systems, Madison, WI 53711, USA, [c]Molecular Biology and Biochemistry, University of California, Irvine, CA 92697, USA, [d]Hampton Research, Aliso Viejo, CA 92656, USA, and [e]q.e.d. life science discoveries, Livermore, CA 94551, USA. Correspondence e-mail: bernhardrupp@sbcglobal.net

High-throughput crystallography has reached a level of automation where complete computer-assisted robotic crystallization pipelines are capable of cocktail preparation, crystallization plate setup, and inspection and interpretation of results. While mounting of crystal pins, data collection and structure solution are highly automated, crystal harvesting and cryocooling remain formidable challenges towards full automation. To address the final frontier in achieving fully automated high-throughput crystallography, the prototype of an anthropomorphic six-axis universal micromanipulation robot (UMR) has been designed and tested; this UMR is capable of operator-assisted harvesting and cryoquenching of protein crystals as small as 10 μm from a variety of 96-well plates. The UMR is equipped with a versatile tool exchanger providing full operational flexibility. Trypsin crystals harvested and cryoquenched using the UMR have yielded a 1.5 Å structure demonstrating the feasibility of robotic protein crystal harvesting.

1. Introduction

Structure-based methods are progressively gaining importance in drug lead discovery and design, and the number of therapeutic drugs developed with major contributions from structure-guided methods is rapidly increasing (Congreve *et al.*, 2006). In particular, automated high-throughput drug target crystallography and associated enabling technologies have contributed significantly towards rational structure-based drug design. Computer-assisted robotic crystallization pipelines are capable of cocktail preparation, crystallization plate setup, and inspection and interpretation of results. The mounting of crystal pins, data collection and structure solution are also highly automated (Karain *et al.*, 2002; Pflugrath, 2004; Snell *et al.*, 2004; Beteva *et al.*, 2006), and more and more beamlines are being equipped with pin mounting robotics (http://smb.slac.stanford.edu/robosync/). Numerous pharmaceutical companies have thus implemented powerful crystallography pipelines, capable of screening numerous drug targets and receptor-ligand complexes per day (Blundell *et al.*, 2002; Hosfield *et al.*, 2003; Congreve *et al.*, 2006).

In contrast to the screening-related liquid- and plate-handling tasks, as well as the manipulation of crystals once they are cryoquenched, the actual harvesting of the crystals is still performed with manual tools under a microscope. The effect of this break in the automation pipeline is manifold: in addition to the creation of a process bottleneck, particularly in pharmaceutical receptor-ligand screening and crystallographic fragment screening (Burley, 2004), the critical harvesting operations occur late in the process and are a major source of loss of valuable crystals. Avoiding expensive late-stage failure during harvesting is a major step towards increased process efficiency and cost reduction (Rupp, 2003). Moreover, the physics of cryocooling (Garman, 1999; Nave & Garman, 2005) are still one of the least well understood areas in protein crystallography. To a large degree, the difficulty in exploring cryoprocedures is rooted in the poor reproducibility of skill-dependent manual harvesting. Consistent robotic or robot-assisted harvesting, combined with novel hyperquenching techniques (Warkentin *et al.*, 2006), will thus impact our ability to systematically optimize cryotechniques for faster, more reliable crystal cooling.

In a first stage towards fully automated high-throughput crystallography, we have designed and tested an anthropomorphic six-axis universal micromanipulation robot (UMR) capable of reliably harvesting and cryoquenching protein crystals as small as 10 μm from a variety of 96-well plates. The UMR arm is equipped with a versatile tool exchanger. Tape cutters, harvesting pins with MiTeGen MicroLoops (Thorne *et al.*, 2003), cryoliquid exchange and custom tools provide additional operational flexibility. The current user interface is a simple game-style keyboard layout allowing intuitive manual control. Semi-automated process steps such as tool location, loop approach to crystals, as well as fully automated tape cutting and quenching have been implemented in the prototype. Integrated machine vision and object tracking are in

development to achieve minimally supervised automated crystal harvesting.

In a first demonstration of operator-assisted robotic operation, we have harvested and cryoquenched a series of 32 different crystals (lysozyme, concanavalin A, glucose isomerase and bovine trypsin) from 96-well sitting-drop plates (1 µl drops) used in automated crystallization pipelines as well as from 24-well CrysChem plates (2 + 2 µl drops) used for manual sitting-drop setup. A movie showing operator-assisted harvest of a ~80 µm lysozyme crystal from a 96-well plate is available from http://www.ruppweb.org/cryscam/lysocapture.wmv. A bovine trypsin crystal harvested using the UMR yielded 1.50 Å-resolution data and a well refined structure with an R value of 0.153 and an $R_{\rm free}$ of 0.176. To our knowledge, this is the first structure from a crystal that has not been directly manipulated by human operators during harvesting and quenching, and it seems to be among the highest resolution trypsin structures refined from in-house data.

Contributing to the high resolution of our trypsin structure is probably the fact that the crystals were grown under conditions that included additives believed to assist in forming crystal contacts (McPherson & Cudney, 2006). The backbone trace of a fragment presumed to be a salmon protamine peptide is visible in weak electron density intercalated between three symmetry-related trypsin molecules.

2. The universal mounting robot

For a robot to harvest protein crystals successfully, it is essential that it be able to mimic the subtle dexterous motions of a human technician. Furthermore, the robot needs to have motion resolutions at least one order of magnitude finer than the diameter of the smallest crystals it will be required to handle. We determined that a six-axis robot with articulated arm geometry was the best choice for this application. Commercial robots are generally not required to operate in the micrometer realm, so the need for special modifications to this robot's actuators, encoders and mechanical linkages was anticipated. As outlined above, we sought to endow the system with a broad range of operational capabilities by equipping it with an automated tool exchange capability and providing access to a library of task-specific end effectors. A video camera with motorized zoom lens provided the system's operator with a high-resolution image of the work volume within a well. The goal was to create a rugged, in the first development phase tele-operated, robotic work cell capable of efficiently performing the full range of tasks associated with crystal harvesting.

2.1. Concept and design

The design team chose the Stäubli RX60 (Fig. 1) as the core robotic component for this application. This Swiss-made robot has been used successfully in a number of very high-precision applications and was deemed to offer the best combination of payload, reach and resolution. Other than minor modifications made to the transmission linkages at the factory, this was an 'off-the-shelf' robot. Initial testing of the robot demonstrated its ability to translate the tip of a standard sample pin with a resolution consistent with the needs of crystal harvesting. Consequently, no further modifications were made to the robot.

Special end effectors were designed to provide for plate handling, tape cutting and crystal harvesting (Fig. 2). In each instance, these designs simply adapted existing manual process tools and provided a means for precisely aligning these tools relative to the robot. Each end effector incorporated kinematic mounting features allowing it to be accurately registered in a storage library at the edge of the work cell. Testing confirmed the system's ability to reliably perform all basic material handling tasks.

Initial tests of the system's ability to harvest crystals were performed using relatively large (~200 µm) lysozyme crystals grown in a sitting-drop configuration. With some practice, an operator was able to capture these crystals successfully *via* the robot's keyboard-driven user interface. Tests were performed using both standard nylon loops provided by Hampton Research and etched Kapton loops manufactured by MiTeGen (Thorne *et al.*, 2003). While both types of loops worked, the Kapton loops were easier to manipulate relative to the crystal and allowed the capture sequence to be performed more quickly. In subsequent tests, only Kapton loops were used.

The next sequence of tests verified the system's ability to capture crystals within a variety of sitting-drop wells. As with the hanging-drop experiments, some practice was needed before an operator was able to maneuver the tip of the harvesting loop efficiently within the geometry of a well. However, once these maneuvers were perfected, tele-operated capture was rapid and reliable (Fig. 3). With this success, progressively smaller lysozyme crystals were harvested, culminating in the capture of crystals only 10 µm in diameter.

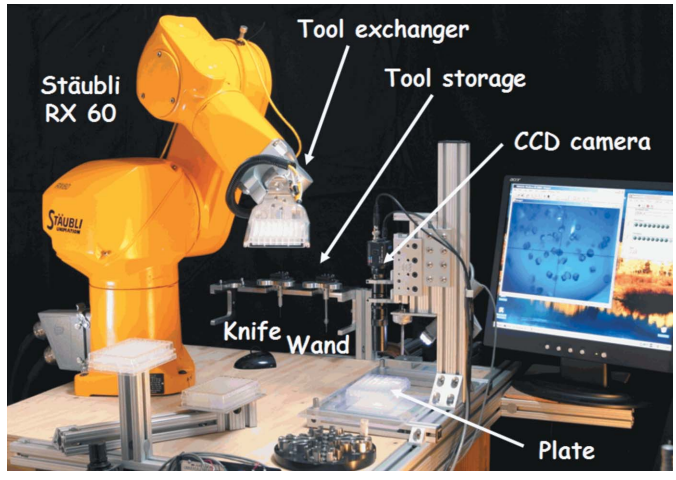

Figure 1
The UMR prototype. The core of the system is a Stäubli RX 60 anthropomorphic six-axis robot, equipped with a versatile pneumatically operated tool exchanger, giving the robotic arm access to a wide range of harvesting loops, microtools and liquid exchange capability.

The feasibility of robotic crystal cleaving and other microsurgical operations were also verified.

2.2. Operational tests and system integration

Following successful demonstration of the robot's ability to perform individual process tasks, system-level tests of the UMR were performed. The goal of these tests was to demonstrate the ability of the UMR to seamlessly perform the sequence of tasks required to completely open the bottleneck associated with the crystal harvesting process. Microtiter plates enter the system through an input port, where the robot accepts the tray and presents it to the imaging module. Magnified images of each of the plate's wells are acquired and displayed to the system operator. Once the operator identifies those wells that hold usable crystals, the robot precisely cuts through the tape, acquires the appropriately sized harvesting loop and positions the tip of the loop in the center of the well. The operator then takes direct control of the robot and performs the necessary harvesting and cryoprotecting operations. Finally, the operator returns control back to the robot and the robot automatically cryoquenches the crystal (Fig. 4). During a series of tests with numerous crystals grown in varying plates under different conditions, the feasibility of a tele-operated UMR was established. Ultimately, a crystal structure of trypsin complexed with benzamidine was refined at 1.5 Å from data collected from a robotically harvested and cryoquenched crystal.

2.3. Future developments

Following the success of the tele-operated harvesting, we will now attempt to expand the functionality of the UMR concept and establish its ability to perform the full range of crystal harvesting tasks autonomously. Refinement of the tele-operated prototype, verification of an appropriately resolved sensory capability (machine vision in this case) and successful conversion of operator-directed robot commands into well

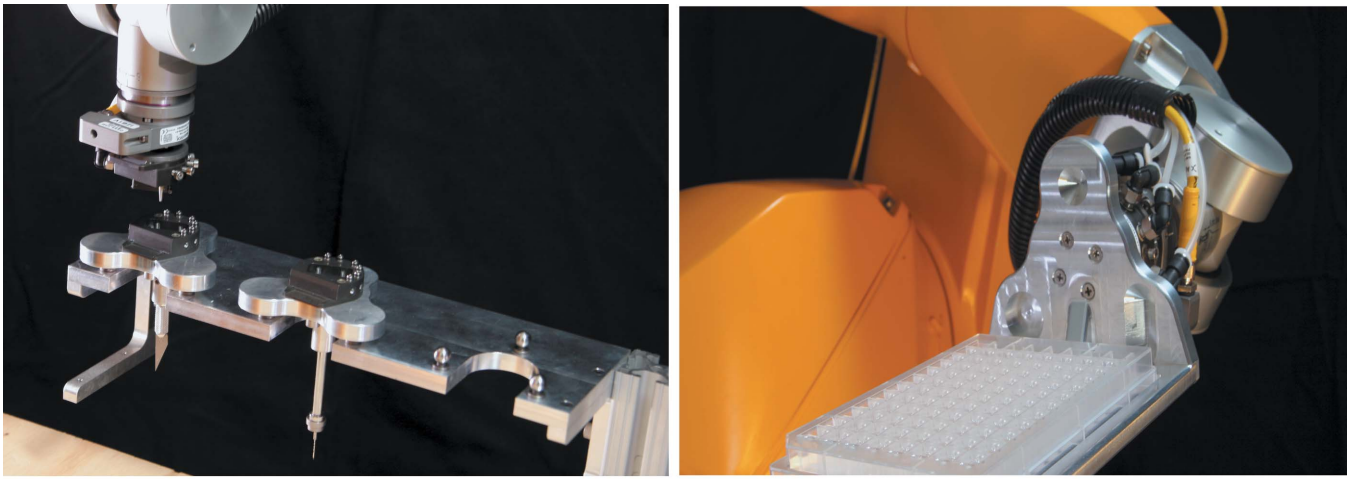

Figure 2
Detailed view of the tool exchanger and tool storage (left panel), and the plate manipulator tool attached to the tool exchanger (right panel).

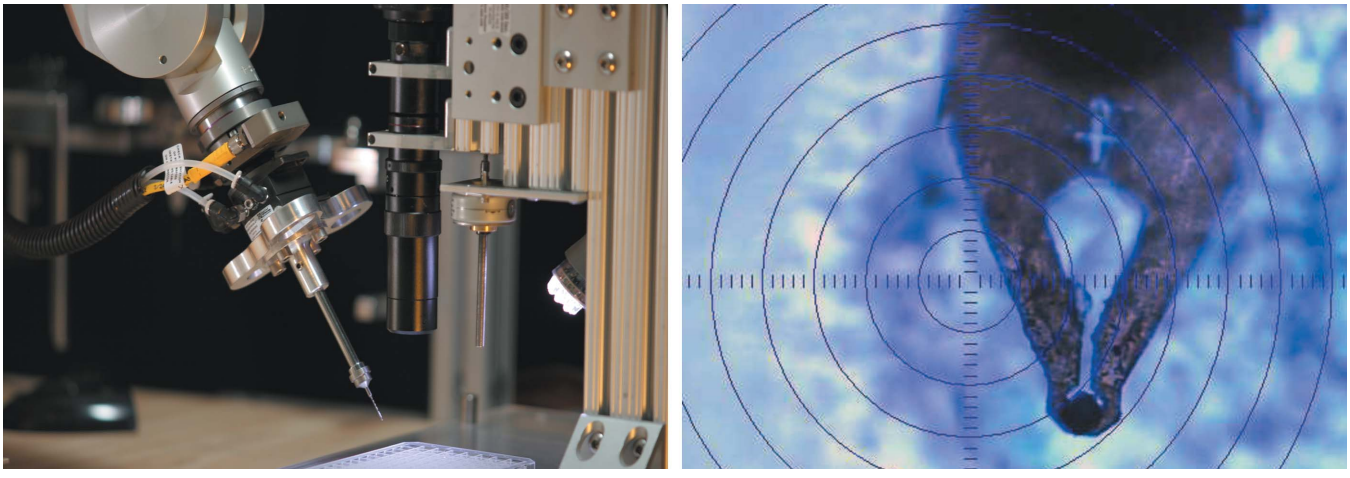

Figure 3
Tool exchanger with harvesting wand carrying a magnetic base Hampton Research CrystalCap pin with Kapton cryo-loop (left panel). A harvested 30 µm lysozyme crystal dyed with methylene blue in the MiTeGen harvesting loop is shown in the right panel.

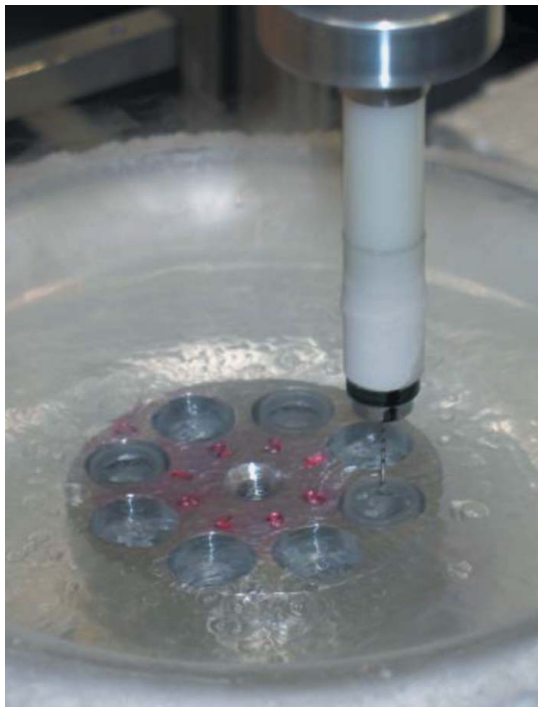

Figure 4
Automated cryoquenching of a crystal in liquid nitrogen. The sample magazine used during the tests was a simplified version of the 'cryo-pucks' currently in use at a number of synchrotron light sources. Because of the system's inherent flexibility, the UMR can be configured for compatibility with any type of storage magazine currently in use.

defined automated motion routines are the three crucial elements needed to create a self-directed system; we plan to investigate each of these elements systematically. Next, a fully realized UMR with expanded functional capabilities will be built and tested. The primary goal of this phase of the project will be to unite the precision robotics already developed with refined machine vision guidance in order to remove the human operator entirely from the crystal harvesting process. Higher-order micromanipulation devices will also be investigated in an effort to lower the system's crystal capture threshold below 1 µm, which will allow harvesting of even the smallest crystals and added precision in micromanipulation procedures, such as dissecting macroscopically twinned or inter-grown crystals. While crystals smaller than 10 µm are of limited value for routine diffraction (generally requiring data collection on specialized microfocusing beamlines), microcrystals may still be useful for seeding operations. Fluid handling will be incorporated into the UMR allowing the system to apply cryoprotectants to mature crystals and to create protein-ligand complexes. Full support of hyperquenching cryotechniques (Warkentin *et al.*, 2006) will significantly extend the conditions under which crystals can be successfully cryomounted. The system's capability to perform necessary 'pedestrian' functions such as plate handling, plate positioning, tape piercing and resealing will also be refined.

One of the most relevant issues for harvesting from small drops (drops in the 100 + 100 µl range are routinely used in robotic setup) is the time needed for harvesting. Tool exchange is very fast (3–5 s) and movement of tools into close proximity of crystals can be performed with high motor speed settings, which will allow the reduction of open well time substantially, while at the same time delicate movements involving crystals can be preformed with great accuracy and consistency. Tool handling is generally very fast and simple for the UMR robot. As a typical example, the change of the harvesting loop from one hand to the other, required by a change in approach position to the well, is difficult even for an ambidextrous operator. For the UMR, only a trivial tool rotation is involved. We think that optimization and automation of numerous steps using the UMR will ultimately minimize harvest times and thus drastically reduce the risk of dried-up crystallization drops before the operation can be completed.

3. Structure of robotically harvested trypsin–benzamidine complex

3.1. Crystallization

Bovine trypsin (60 mg, Sigma Chemicals) was mixed with benzamidine (5 mg, Sigma Chemicals) and dissolved in 1 ml of 0.1 *M* HEPES buffer at pH 7.0 containing 3 m*M* $CaCl_2$. The protein–benzamidine complex was then crystallized by sitting-drop vapor diffusion (McPherson & Cudney, 2006) in Cryschem plastic plates (Hampton Research, Aliso Viejo, CA). The sample drops were composed of 2 µl of the protein–benzamidine stock and 2 µl of 15% PEG 3350 in 0.1 *M* HEPES pH 7.0, also containing 10 mg ml^{-1} of salmon sperm protamine (Sigma Chemicals). The sample yielded orthorhombic prismatic crystals after about one week at 295 K.

3.2. Robotic harvesting and cryocooling

The sitting-drop plate containing trypsin crystals was loaded into the UMR and positioned relative to the imaging optics. Candidate crystals were identified by the system's operator and robotically harvested as described in §2 using an appropriately sized Kapton loop. Immediately following capture, the crystals were quenched in liquid nitrogen and inserted into a cryostorage puck as depicted in Fig. 4.

3.3. Data collection

Hampton Research CrystalCap pins containing the cryoprotected robotically harvested crystals in MiteGen Kapton loops (Thorne *et al.*, 2003) were directly mounted out of liquid-nitrogen storage pucks using cryo-tongs. Diffraction data of the orthorhombic $P2_12_12_1$ crystals were collected in anomalous data collection strategy at 100 K with a Platinum^{135} CCD detector using Cu $K\alpha$ radiation from a Bruker MICROSTAR-H rotating-anode generator operating at 2.7 kW. Intensities were integrated and scaled using the *PROTEUM* software suite (Bruker, 2004). Data collection statistics are summarized in Table 1.

Table 1
Data collection and refinement statistics.

Data collection	
Space group	$P2_12_12_1$
Wavelength (Å)	1.54178
a (Å)	53.92
b (Å)	56.70
c (Å)	66.05
Resolution (Å)	25.09–1.50 (1.57–1.50)
Unique reflections	31641 (2099)
Redundancy	7.46 (3.32)
Completeness	99.3 (95.9)
R_{sym}	0.0471 (0.3106)
$\langle I/\sigma(I)\rangle$	24.37 (3.84)
Number of molecules in a.u.	1
V_m (Matthews coefficient)	2.03
% Solvent	39.1
Refinement	
Free *R* value†, random, 5%	0.176 (0.281)
R value†	0.156 (0.198)
r.m.s.d. bond length (Å)‡	0.012
r.m.s.d. bond angle (°)‡	1.394
Overall coordinate error (Å)§	0.068
RSCC (*Shake & wARP*)¶	0.96
RSCC (*REFMAC5*)††	0.97
EDS map *R*value‡‡	0.177
Ramachandran appearance§§ nonglycine	
Most favored region (residues, %)	164 (87.2)
Additional allowed (residues, %)	24 (12.8)
Generously allowed (residues, %)	0
Disallowed (residues, %)	0

† Values in parentheses for the highest resolution bin in refinement (1.54–1.50 Å). ‡ Deviations from restraint targets (Engh & Huber, 1991). § Estimated standard uncertainty, diffraction precision index (DPI) based on R_{free} (Cruickshank, 1999). ¶ Real-space correlation coefficient, F_c map against averaged and weighted *Shake & wARP* map. †† Real-space correlation coefficient, F_o map against F_c map, as reported by *REFMAC5*. ‡‡ Returned by EDS validation server (Kleywegt *et al.*, 2004) during deposition *via* autodep (EBI-MSD). §§ Regions as defined in *PROCHECK* (Laskowski *et al.*, 1993).

3.4. Structure solution and refinement

The processed diffraction data in *SCALEPACK* (Otwinowski & Minor, 1997) format and the starting model (PDB code 1v2l) were submitted to the *Shake & wARP* (*SNW*) package (Reddy *et al.*, 2003) for molecular replacement, rigid-body refinement and generation of multiple-averaged bias minimized *SNW* maps. Manual adjustment and rebuilding in *Xtalview* (McRee, 1999) and *Coot* (Emsley & Cowtan, 2004) was followed by maximum-likelihood refinement in *REFMAC5* (Murshudov *et al.*, 1997). After building of water structure and repeated bias removal using *SNW*, further features in the electron density could be built. We placed the inhibiting benzamidine in its unambiguous electron density and built phenol molecules, presumably originating from the protamine preparation, in two alternate conformations in corresponding density. At this stage, real-space correlation of the trypsin model was excellent (Fig. 2), R_{free} was 18.3, and weak but in large parts contiguous electron density could be detected between neighboring molecules in both *SNW* and mF_o–Df_c maps.

The residual density was approximated as the backbone trace of a peptide, probably resulting from the salmon protamine extract and built as polyglycine. At several Cα positions, adjacent Cβ density was present, but no sequence assignment was possible. Although R_{free} dropped to 0.176 after final refinement (R = 0.153), the exact conformation and nature of the peptide remains undetermined. A water molecule in an octahedral environment showed positive difference density and refined to low B values, suggesting a second metal binding site in addition to the constitutive Ca^{2+} ion in trypsin. A phased anomalous difference map showed a weak peak, and based on bond distances a sodium ion was placed in the density as a probable cation, although partial occupation by other cations cannot be excluded. There were no indications of anisotropy in the electron density maps, and neither TLS refinement nor partial introduction of anisotropic B factors led to significant improvements in R_{free}. Refinement statistics, coordinate r.m.s.d. and geometry statistics are compiled in Table 1. In a final polishing step, all Asn, Gln and His side-chain conformations were checked for chemical plausibility (Weichenberger & Sippl, 2006), and close distance deviations (bumps) of more than 0.2 Å from *WHATCHECK* targets were corrected (Hoft *et al.*, 1996). Coordinates and structure factors (code 2j9n) have been deposited with the Protein Data Bank and validated during deposition at EBI-MSD *via* autodep and the EDS (Kleywegt *et al.*, 2004) service.

3.5. Packing analysis of trypsin

Trypsin is a hardy perennial of protein crystallography, and atomic resolution structures of trypsin, particularly of *Fusarium oxysporum* (Schmidt *et al.*, 2003), have been used to analyze details of the reaction pathway and molecular movements in the enzyme. Crystals of benzamidine-complexed trypsin ($K_d \simeq 20\ \mu M$) served as a model in the recently developed radiation-induced phasing (RIP) technique (Nanao *et al.*, 2005). Nearly 260 structures of trypsin from various species, complexed with other inhibitors, and in substrate complexes have been determined (compiled in the REMARK 900 section of PDB entry 2j9n).

Trypsin is a member of the ubiquitous family of serine proteases. It is secreted by the pancreas as the proenzyme trypsinogen and converted to the active form in the small intestine by enteropeptidase. As an *endo*-petidase, active trypsin cleaves substrates at the C-terminal of Arg and Lys, and catalyzes the cleavage and activation of additional trypsinogen and other pancreatic proenzymes important to protein digestion. The calytic triade in the binding pocket consists of Ser, His and Asp (residues 192, 55 and 99 in our model).

3.5.1. Binding site environment. Comparison with a representative atomic resolution structure (in the orthorhombic $P2_12_12_1$ crystal form with cell constants of ~54, 57 and 66 Å) of bovine trypsin in complex with the competitive inhibitor benzamidine (PDB entry 1j8a; Cuesta-Seijo & Garcia-Granda, 2002) shows excellent overall agreement (superposition with 0.23 Å overall r.m.s.d.). The binding site contains the benzamidine inhibitor, fully occupied and in a position practically identical to that in other high-resolution

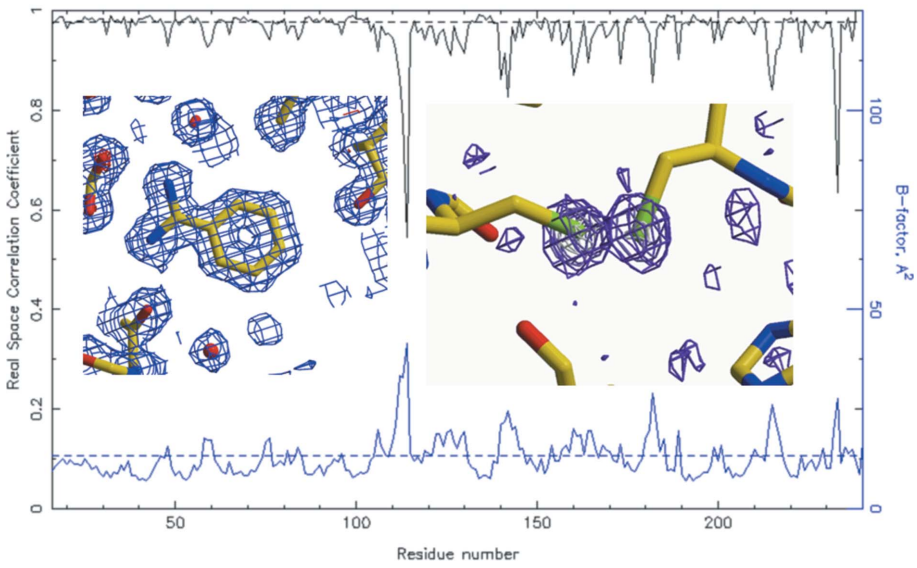

Figure 5
Real-space correlation coefficients against a bias-minimized *SNW* map (black) and *B* factors (blue) for the final model of trypsin 2j9n, demonstrating the quality of the trypsin model obtained from the robotically harvested crystals. Inserts shows *SNW* omit electron density of the benzamidine inhibitor (left) and the phased anomalous difference map of the disulfide bond Cys40—Cys56. Density figures were generated using *Xfit* (McRee, 1999) and *Raster3d* (Merritt & Bacon, 1997).

structures (Fig. 5). A number of water molecules in the binding site are also conserved, amongst those the W1 water molecule (next to the histidine of the catalytic triade), shown to act as nucleophile in the cleavage reaction (Schmidt *et al.*, 2003). In the $P2_12_12_1$ crystal form typical for trypsin inhibited with the arginine analogue benzamidine, the position of the natural peptide substrates is occupied by a symmetry-related molecule (Fig. 6).

3.5.2. Intercalating density. Of particular interest in our structure are the nature and location of the intermolecular entities connecting three neighboring molecules in the $P2_12_12_1$ structure. Bias-minimized *SNW* electron density maps (Reddy *et al.*, 2003) as well as maximum-likelihood/SigmaA mf_o–Df_c (DELFWT) maps created with *REFMAC5* (Murshudov *et al.*, 1997) show distinct density fragments, which at lower contour levels of 0.7–0.5σ became contiguous over a large distance equivalent to more than 20 amino acid residues. Given that the main additive in the crystallization cocktail was a salmon protamine extract (SPE), there are several possibilities of which macromolecular entities could be located between the molecules. SPE contains various highly cationic peptides, generally basic and arginine rich, as well as other potential components such as polyamines of the spermidine/spermine family. The fact that the electron density, despite the high resolution of the remaining structure, did not show side-chain features distinct enough to allow a clear assignment of residues and directionality seems to indicate that a mixture of peptides in multiple conformations, possibly also polyamines in the region where no side chains can be accommodated, are linking the molecules.

There is in fact precedence for intermolecular contact mediation of protamine peptides in crystal structures. Strikingly similar fragments have been located in crystal interfaces of insulin in drug formulations containing the protamine clupeine (Balschmidt *et al.*, 1991). Interestingly, in this insulin structure, a phenol derivative (*m*-cresol) has also been found to mediate crystal contacts, and phenol has been used to stabilize other insulins (Derewenda *et al.*, 1989). In the absence of a clear assignment, we have modeled our density as a three- and a 16-residue polyglycine backbone (possibly led by an N-terminal lysine residue) as a placeholder for what is probably a mixture of intercalated peptides and other SPE components. Unassigned density that could correspond to the guanidyl groups of arginine in the vicinity of acidic residues and hydrogen-bond acceptors has been observed, but ordered side chains could not be built, probably as a consequence of the substantial entropic loss that would accompany rigid arginine conformations. The averaged *B* factors (~70 Å^2) of the peptides are accordingly higher than those of surface-exposed trypsin residues (~16 Å^2), indicating partial occupation and/or disorder. To emphasize the tentative assignment, we used the residue name UNK for these peptides in the PDB file.

Despite the weak density, our intercalated model trace displays features that are compatible with an arginine- and lysine-rich basic peptide; as shown in Fig. 7, the peptide density snakes though the interface between the molecules so that its basic side chains would indeed make contacts with negatively charged patches on the molecules, whereas back-

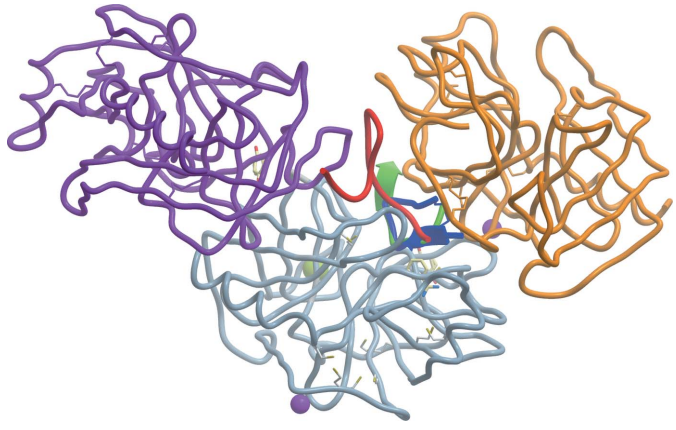

Figure 6
Packing of trypsin molecules with intercalating peptide. Two symmetry-related molecules are shown in purple and yellow; the peptide linking the three molecules is shown in red. In addition, residues of BPTI (green; PDB code 3btd; Helland *et al.*, 1999) and a synthetic peptide inhibitor (blue; PDB code 1ox1) are superimposed on the central trypsin (grey), showing that the intercalating density occupies a different location from the peptide substrates. Figure prepared with *ICM Pro* Version 3.7 (Abagyan *et al.*, 1994).

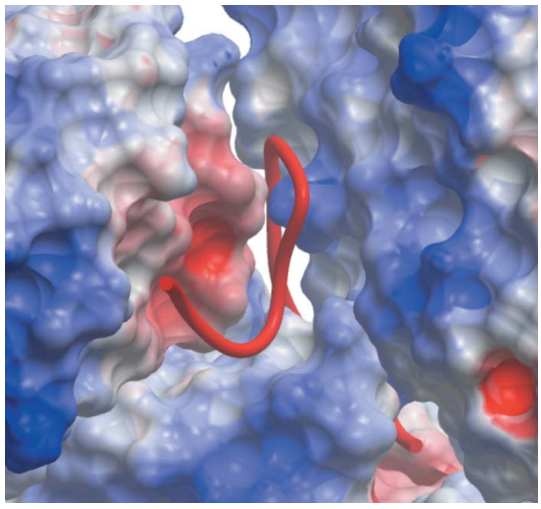

Figure 7
Enlarged section of the interface region between three trypsin molecules (same orientation as Fig. 6). The trace of the peptide (red) shows that it is located so that its positively charged side chains such as arginine and lysine would generally interact with negative patches on the trypsin surface (red) while interactions of the peptide backbone involve basic residues (blue) of the neighboring molecule's residues. Figure prepared using *ICM Pro* Version 3.7 (Abagyan *et al.*, 1994).

bone contacts were generally observed to the polar amide residues of trypsin. *LIGPLOT* analysis (Wallace *et al.*, 1995) (not shown) of the hydrogen-bond network between trypsin molecules and the backbone of the intercalated peptide verified that the intermolecular contacts involve all three neighboring trypsin molecules.

4. Summary

We have conclusively demonstrated that protein crystals can be successfully harvested and cryoquenched using advanced micromanipulation robotics. Future developments will be targeted towards increasingly autonomous operations with fully integrated real-time machine vision support. Ultimately, the integration of the UMR into robotic protein crystallization pipelines will enable the vision of fully automated protein crystallization platforms as the core of high-throughput crystallography in structural genomics and in pharmaceutical drug target crystallography.

This work was sponsored under NIH STTR Phase I grant No. 1 R41 GM073278-01 and by contributions from Square One Systems Design, WY; Bruker AXS, WI; Hampton Research, CA; and q.e.d. life science discoveries, CA. We thank the EBI-MSD deposition team for the careful annotation of PDB entry 2j9n.

References

Abagyan, R., Totrov, M. & Kuznetsov, D. (1994). *J. Comput. Chem.* **15**, 488–506.
Balschmidt, P., Hansen, F. B., Dodson, E. J., Dodson, G. G. & Korber, F. (1991). *Acta Cryst.* B**47**, 975–986.
Beteva, A. *et al.* (2006). *Acta Cryst.* D**62**, 1162–1169.
Blundell, T. L., Jhoti, H. & Abell, C. (2002). *Nat. Rev. Drug Discov.* **1**, 45–54.
Bruker (2004). *PROTEUM*. Bruker AXS Inc., Madison, Wisconsin, USA.
Burley, S. (2004). *Modern Drug Discov.* **7**, 53–56.
Congreve, M., Murray, C. & Blundell, T. (2006). *Drug Discov. Today*, **10**, 895–907.
Cruickshank, D. W. J. (1999). *Acta Cryst.* D**55**, 583–601.
Cuesta-Seijo, J. A. & Garcia-Granda, S. (2002). *Bol. R. Soc. Hist. Nat. Sec. Geol.* **97**, 123–131.
Derewenda, U., Derewenda, Z., Dodson, E. J., Dodson, G. G., Reynolds, C. D., Smith, G. D., Sparks, C. & Swenson, D. (1989). *Nature* (*London*), **338**, 594–596.
Emsley, P. & Cowtan, K. (2004). *Acta Cryst.* D**60**, 2126–2132.
Engh, R. A. & Huber, R. (1991). *Acta Cryst.* A**47**, 392–400.
Garman, E. (1999). *Acta Cryst.* D**55**, 1641–1653.
Helland, R., Otlewski, J., Sundheim, O., Dadlez, M. & Smalas, A. O. (1999). *J. Mol. Biol.* **287**, 923–942.
Hoft, R. R. W., Vriend, G., Sander, C. & Albola, E. E. (1996). *Nature* (*London*), **381**, 272.
Hosfield, D., Palan, J., Hilgers, M., Scheibe, D., McRee, D. E. & Stevens, R. C. (2003). *J. Struct. Biol.* **142**, 207–217.
Karain, W. I., Bourenkov, G. P., Blume, H. & Bartunik, H. D. (2002). *Acta Cryst.* D**58**, 1519–1522.
Kleywegt, G. J., Harris, M. R., Zou, J.-Y., Taylor, T. C., Wahlby, A. & Jones, T. A. (2004). *Acta Cryst.* D**60**, 2240–2249.
Laskowski, R. A., MacArthur, M. W., Moss, D. S. & Thornton, J. M. (1993). *J. Appl. Cryst.* **26**, 283–291.
McPherson, A. & Cudney, B. (2006). *J. Struct. Biol.* **156**, 387–406.
McRee, D. E. (1999). *J. Struct. Biol.* **125**, 156–165.
Merritt, E. A. & Bacon, D. J. (1997). *Methods Enzymol.* **277**, 505–524.
Murshudov, G. N., Vagin, A. A. & Dodson, E. D. (1997). *Acta Cryst.* D**53**, 240–255.
Nanao, M. H., Sheldrick, G. M. & Ravelli, R. B. (2005). *Acta Cryst.* D**61**, 1227–1237.
Nave, C. & Garman, E. (2005). *J. Synchrotron Rad.* **12**, 257–260.
Otwinowski, Z. & Minor, W. (1997). *Methods Enzymol.* **267**, 307–326.
Pflugrath, J. W. (2004). *Methods*, **34**, 415–423.
Reddy, V., Swanson, S., Sacchettini, J. C., Kantardjieff, K. A., Segelke, B. & Rupp, B. (2003). *Acta Cryst.* D**59**, 2200–2210.
Rupp, B. (2003). *Acc. Chem. Res.* **36**, 173–181.
Schmidt, A., Jelsch, C., Ostergaard, P., Rypniewski, W. & Lamzin, V. S. (2003). *J. Biol. Chem.* **278**, 43357–43362.
Snell, G., Cork, C., Nordmeyer, R., Cornell, E., Meigs, G., Yegian, D., Jaklevic, J., Jin, J., Stevens, R. C. & Earnest, T. E. (2004). *Structure*, **12**, 1–12.
Thorne, R. E., Stum, Z., Kmetko, J., O'Neill, K. & Gillilan, R. (2003). *J. Appl. Cryst.* **36**, 1455–1460.
Wallace, A. C., Laskowski, R. A. & Thornton, J. M. (1995). *Protein Eng.* **8**, 127–134.
Warkentin, M., Berejnov, V., Husseini, N. S. & Thorne, R. E. (2006). *J. Appl. Cryst.* **39**, 805–811.
Weichenberger, C. X. & Sippl, M. J. (2006). *Structure*, **14**, 967–972.